



1 Quantifying Temperature-sliding Inconsistency in Thermomechanical Coupling: A
2 Comparative Analysis of Geothermal Heat Flux Datasets at Totten Glacier

3

4 Junshun Wang¹, Liyun Zhao¹, Michael Wolovick², John C. Moore³

5 ¹State Key Laboratory of Earth Surface Processes and Hazards Risk Governance
6 (ESPHR), Faculty of Geographical Science, Beijing Normal University, Beijing
7 100875, China

8 ²Glaciology Section, Alfred-Wegener-Institut, Helmholtz-Zentrum für Polar- und
9 Meeresforschung, Bremerhaven, Germany

10 ³Arctic Centre, University of Lapland, Rovaniemi, Finland

11 *Correspondence:* Liyun Zhao (zhaoliyun@bnu.edu.cn), John C. Moore
12 (john.moore.bnu@gmail.com)

13

14

15

16 **Abstract.** Rapid sliding of ice sheets requires warm basal temperatures and lubricating
17 basal meltwater, whereas slow velocities typically correlate with a frozen bed. However,
18 ice sheet models often infer basal sliding by inverting surface velocity observations
19 with the vertical structure of temperature and hence rheology held constant. If the
20 inversion is allowed to freely vary sliding over the model domain, then inconsistencies
21 between the basal thermal state and ice motion can arise lowering simulation realism.
22 In this study, we propose a new method that quantifies inconsistencies when inferring
23 warm and cold-bedded regions of ice sheets. This method can be used to evaluate the
24 quality of ice sheet simulation results without requiring any englacial or subglacial
25 measurements. We apply the method to evaluate simulation results for Totten Glacier
26 using an isotropic 3D full-Stokes ice sheet model with eight geothermal heat flux (GHF)
27 datasets and compare our evaluation results with inferences on basal thermal state from
28 radar specularity. The rankings of GHF datasets based on inconsistency are closely
29 aligned with those using the independent specularity content data. Examples of the
30 method utility are 1. an inconsistency characterizing overcooling with all GHFs near
31 the western boundary of Totten Glacier between 70°S-72°S, where there is a bedrock
32 canyon and fast surface ice velocities, which suggests that GHF is low in all published
33 datasets; 2. an overheating inconsistency in the eastern Totten Glacier with all GHFs
34 that leads to overestimation of ice temperature due, in this case, to an unrealistically
35 warm surface temperature. Our approach opens a new avenue for assessing the self-
36 consistency and reliability of ice sheet model results and GHF datasets, which may be
37 widely applicable.



38 **1. Introduction**

39 Ice sheet models are an important tool for projections of ice sheet mass balance
40 and their contribution to sea level rise. Ice sheet models are usually initialized by “spin-
41 up” or data assimilation such that they reproduce the present-day geometry or surface
42 velocity of an ice sheet (Seroussi et al., 2019). Often ice sheet model simulations derive
43 ice dynamics using ice temperatures taken from other studies (e.g., Gillet-Chaulet et al.,
44 2012; Van Liefferinge and Pattyn, 2013; Cornford et al., 2015; Pittard et al., 2016;
45 Siahaan et al., 2022). In thermo-mechanically coupled ice sheet simulations, the ice
46 sheet model is usually spun up with idealized temperature-depth profiles and then run
47 in a thermo-mechanically coupled mode constrained by geothermal heat flux (GHF)
48 and surface ice temperature fields (Seroussi et al., 2019). While advances in satellite
49 and field observation technologies have led to a preliminary consensus on ice sheet
50 geometry and surface ice temperature, significant uncertainties persist in basal
51 boundary conditions, including GHF and basal friction, since reliable observational
52 data are scarce. These basal properties introduce significant uncertainty in the simulated
53 ice sheet dynamics, and thus ice sheet mass balance.

54 The GHF, the heat flow from the Earth's crust to the base of ice sheet, is a critical
55 variable in the basal boundary condition for simulating the ice temperature profile, and
56 hence ice rheology and flow dynamics (Fisher et al., 2015; Smith - Johnsen et al., 2020;
57 Reading et al., 2022). Several GHF datasets exist, derived in various ways from
58 geophysical observations and models, and they exhibit significant variability in both
59 spatial distribution and magnitude (e.g., An et al., 2015; Dziadek et al., 2017; Martos et
60 al., 2017; Shen et al., 2020; Stål et al., 2021). These GHF datasets have been widely
61 used in thermodynamic simulations of Antarctica (e.g., McCormack et al., 2022;
62 Shackleton et al., 2023; Park et al., 2024; Van Liefferinge et al., 2018). However,
63 assessing the GHF field accuracy is problematic because in situ measurements such as
64 boreholes are sparse. Few studies have assessed the quality and reliability of GHF
65 datasets over specific regions. Kang et al. (2022) employed a combination of forward
66 model and inversion using a 3D full-Stokes ice flow model to simulate the basal thermal
67 state in the Lambert–Amery Glacier region and evaluate different GHFs using the
68 locations of subglacial lakes, but the constraints used were asymmetric between cold
69 and warm beds, and assigned inflated reliability to the warmer GHF maps. Indirect
70 estimates of basal conditions have used airborne radar specularity content (Schroeder
71 et al., 2013, 2015; Young et al., 2016) as proxies for basal wetness/dryness and thermal
72 regime (Dow et al., 2020). Huang et al. (2024) used an inverse modeling approach
73 similar to that of Kang et al. (2022) for Totten Glacier and combined this with measured
74 radar specularity content to derive a two-sided constraint on the basal thermal state in
75 addition to subglacial lakes locations. However, specularity content is not yet available
76 for many regions of Antarctica.



77 The basal friction field is another poorly known boundary condition in ice sheet
78 modeling, and a key source of uncertainty in the long-term projection of ice sheets and
79 glaciers. Although basal slip is crucial to the 3D ice flow, it is difficult to observe.
80 Several basal sliding parameterizations have been proposed and widely used
81 (Weertman, 1957; Kamb, 1970; Nye, 1970; Budd et al., 1979; Fowler, 1981; Schoof,
82 2005; Gagliardini et al., 2007; Gladstone et al., 2014; Tsai et al., 2015; Brondex et al.,
83 2017, 2019). The linear Weertman basal sliding parameterization is the most widely
84 used due to its simple form. Given prescribed or modelled ice temperatures and hence
85 ice viscosity, numerous studies have inferred the spatial distribution of basal friction
86 coefficient over grounded ice to best match observed present-day surface ice velocities
87 or ice sheet geometry using snapshot or time-dependent data assimilation and inverse
88 methods (MacAyeal, 1993; Morlighem et al., 2010; Rignot et al., 2011; Gillet-Chaulet
89 et al., 2012; Larour et al., 2012; Pollard and DeConto, 2012; Morlighem et al., 2013;
90 Perego et al., 2014; Pattyn, 2017; Albrecht et al., 2020; Lipscomb et al., 2021; Choi et
91 al., 2023). However, such inversions typically allow the friction coefficient to vary
92 freely to match the surface velocity observations. This can potentially lead to conflicts
93 with the temperature field used during the inversion, which we refer to as
94 “inconsistencies” in this study. For instance, relatively fast surface ice velocity may
95 demand basal sliding in areas where the basal temperatures are below the local pressure
96 melting point. These inconsistencies may be due to unrealistic ice temperatures or a
97 lack of complete physics in the ice sheet model. However, many studies overlook this
98 aspect, and use the inversion results to initialize ice sheet dynamics simulations and
99 estimate glacier mass balance and its contribution to sea level rise (Seroussi et al., 2019;
100 Peyaud et al., 2020; Schannwell et al., 2020; Payne et al., 2021).

101 To the best of our knowledge, there has been no study of such inconsistencies
102 between simulated ice temperature and observed surface ice velocity. Here we develop
103 a novel and generally applicable method to estimate this inconsistency without relying
104 on basal observation data. We utilize the inconsistency of the modelled ice temperature
105 and observed velocity fields to evaluate the quality of ice flow model results. Notably,
106 this approach can also serve as a supplementary method for assessing geothermal heat
107 flux datasets, relying solely on surface ice velocity observations rather than additional
108 englacial or subglacial data.

109 We apply our method to Totten Glacier, a primary outlet of the Aurora subglacial
110 basin in East Antarctica (Greenbaum et al., 2015; Pritchard et al., 2009). The Totten
111 Glacier subregion experienced the largest mass loss among drainage basins in East
112 Antarctica during the period 1979-2017 and 2003-2020 (Kim et al., 2024; Rignot et al.,
113 2019) (Fig. 1a). We examine inconsistencies between simulated ice temperature and ice
114 velocity fields using a 3D full-Stokes model using the various GHFs included in Huang
115 et al. (2024) and use this analysis to rank the reliability of different GHF fields. This



116 GHF ranking closely resembles that reported by Huang et al. (2024), which used the
117 agreement between the modelled basal thermal regime and specularity content, which
118 we take as a validation of the method. Since the new method does not require any
119 englacial or subglacial data, it can be applied to many glaciers, particularly those
120 lacking observations. Our approach can provide a swift assessment of the plausibility
121 of basal temperature and velocity simulated by ice sheet models. Additionally, it can be
122 effectively utilized to map the spatial distribution of GHF over- or under-estimation.
123

124 **2. Method**

125 The inconsistencies defined in this study are essentially between the modelled
126 basal thermal state and observed surface ice flow motion. More specifically, the
127 inconsistencies are between modelled frozen bed and modelled basal sliding (which is
128 tuned to match the observed fast surface velocity during the inversion), and between
129 modelled warm bed and observed slow surface velocity. The inconsistencies originate
130 from multiple causes, including uncertainties in GHF, surface ice temperature, ice sheet
131 geometry, bed topography, surface velocity, ice density and incomplete ice flow
132 mechanics.

133 There is no direct correlation between basal temperature and surface velocity;
134 rather, they are linked through the basal thermal state - the basal temperature being at
135 or below the pressure melting point. The ice bottom in the study domain can be
136 partitioned into warm and cold beds depending on whether the simulated basal ice
137 temperature reaches the local pressure melting point. To effectively penalize models
138 exhibiting both localized overheating (bed too warm) and overcooling (bed too cold),
139 we establish overheating metrics within the warm-bedded region and overcooling
140 metrics within the cold-bedded region to quantitatively assess the inconsistency
141 between the simulated temperature and velocity fields. Thus, we provide two-sided
142 constraints on the temperature field that penalize both too high and too low ice
143 temperature.

144 Overcooling occurs where basal temperature is underestimated. Crucially, in
145 regions with relatively fast observed surface velocity, the inverse method nevertheless
146 yields a nonzero basal velocity — a physically inconsistent result given the cold basal
147 temperature. When basal ice temperature is below the pressure melting point, the basal
148 modelled velocity is expected to approach zero. This inconsistency is larger for faster
149 simulated basal ice speed and for colder simulated basal temperatures. We therefore use
150 a formula that accounts for both variables to quantify overcooling:

$$151 \quad AOC = (T_{melt} - T_{bm}) \times U_{bm}, \quad (1)$$

152 where AOC stands for absolute overcooling, T_{melt} is the basal pressure melting point,
153 T_{bm} represents the simulated basal ice temperature and U_{bm} means the simulated basal
154 ice speed.



155 For the overheating metric, since the first term of the right-hand side of Eq. (1)
156 becomes zero at a warm bed, we cannot use a similar formula as Eq. (1). It is not
157 straightforward to quantify the inconsistencies between modelled warm bed and
158 expected slow basal speed given slow observed surface speed. We note the fact that
159 modelled basal sliding speed must remain non-negative. If the ice is warm and soft
160 enough to permit deformation such that the modelled surface speed is much faster than
161 the observed, then a friction inversion will be ineffective to correct this misfit,
162 producing a bias towards positive misfits (i.e., model velocities are too fast) in the
163 inversion results. Therefore, we use the positive difference between the simulated
164 surface ice speed and the observed speed to calculate the inconsistency caused by the
165 overheating effect:

166
$$AOH = \max(0, U_{sm} - U_{obs}), \quad (2)$$

167 where AOH refers to absolute overheating, U_{sm} represents the modelled surface ice
168 speed and U_{obs} is the observed surface ice speed. We only calculated AOH for the warm-
169 bedded areas, i.e. $T_{bm} = T_{melt}$, because observed surface ice speed errors are
170 proportionally much less in warm-bedded areas (corresponding to fast flow regions)
171 than in cold-bedded area (correspond to slow flow regions).

172 To mitigate the impact of substantial differences in observed surface ice speed
173 across various areas, we also define "relative overheating" (ROH) and "relative
174 overcooling" (ROC), dividing AOH and AOC by the observed surface ice speed
175 respectively:

176
$$ROH = \frac{\max(0, U_{sm} - U_{obs})}{U_{obs}}, \quad (3)$$

177
$$ROC = (T_{melt} - T_{bm}) \times \frac{U_{bm}}{U_{obs}}. \quad (4)$$

178 The summation of the above four metric values is computed across grid points
179 where each metric is explicitly defined. Specifically, AOH and ROH metrics are
180 computed over the warm bed region, and AOC and ROC metrics are computed over the
181 cold bed region for each simulation result. This summation approach was chosen to
182 preserve the total magnitude of inconsistencies, as the warm bed and cold bed regions
183 are different due to distinct GHF boundary conditions. Furthermore, since all
184 experiments utilize identical mesh, the cumulative values remain directly comparable
185 for cross-experiment analysis. We only consider grounded ice and exclude points
186 located at the domain boundary due to relatively poor model performance there.

187 To evaluate the inconsistencies for the whole domain, we linearly normalized the
188 overheating inconsistency and overcooling inconsistency to range from 0 to 1 and then
189 sum them as:

190
$$ACI = L_N(AOC) + L_N(AOH), \quad (5)$$

191
$$RCI = L_N(ROC) + L_N(ROH), \quad (6)$$



192 where ACI means absolute combined inconsistency, RCI represents relative combined
193 inconsistency, and L_N represents linear normalization. Taking AOC as an example, its
194 linear normalization is:

195
$$L_N(AOC) = \frac{AOC - AOC_{min}}{AOC_{max} - AOC_{min}}. \quad (7)$$

196 where AOC_{min} and AOC_{max} denote the minimal and maximal AOC values across all the
197 simulation results when multiple simulation outcomes are available. Therefore, we
198 obtain 6 metrics consisting of three absolute inconsistencies (AOH , AOC , ACI) and
199 three relative inconsistencies (ROH , ROC , RCI).

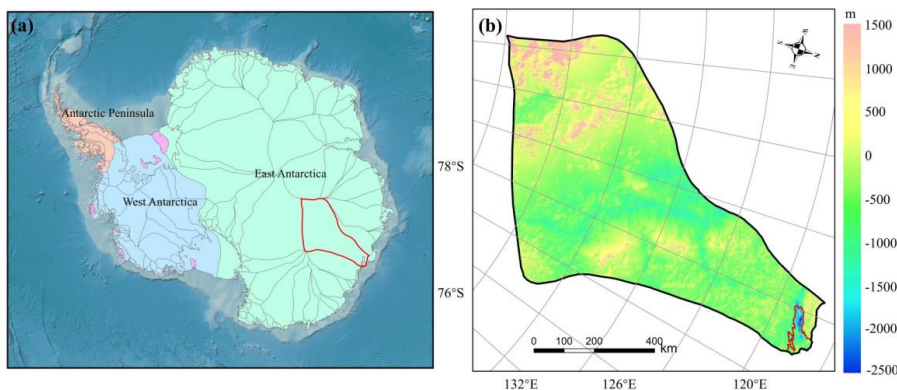
200 These 6 indicators can comprehensively analyze the temperature-sliding
201 inconsistency in the inversion results of ice sheet model. For each metric, simulation
202 results are assigned ranks ranging from 1 to N (where N represents the total number of
203 simulation results), with 1 indicating the smallest inconsistency and N the largest. The
204 final score for each simulation result is subsequently calculated as the arithmetic mean
205 of its six metric-derived scores, ensuring a comprehensive evaluation framework. as a
206 reasonable simulation result should perform well across warm bed, cold bed, and the
207 whole region.

208

209 3. Application to Totten Glacier with Different GHFs

210 3.1 Study domain and Data

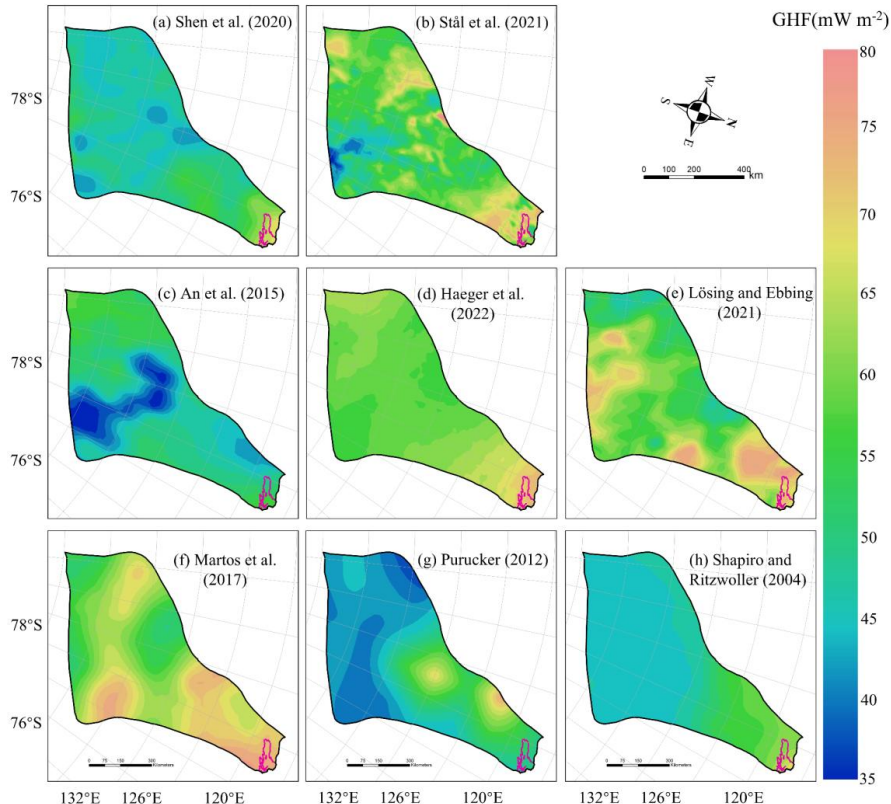
211 We apply our method to evaluate simulated ice temperature and ice velocity in
212 Totten Glacier by following Huang et al. (2024) and using eight GHF datasets. Huang
213 et al. (2024) used the present-day surface ice temperature (Le Brocq et al., 2010) and
214 ice sheet topography data from BedMachine Antarctica, version 2 (Morlighem et al.,
215 2020). The eight GHF datasets were derived by various methodologies, resulting in
216 significant differences in both spatial distribution and magnitude (Fig. 2). GHF fields
217 from Stål et al. (2021), Haeger et al. (2022), Lösing and Ebbing (2021) and Martos et
218 al. (2017) generally exhibit higher magnitudes than the other GHFs.



219



220 **Figure 1.** (a) Geographic location of Totten Glacier (red outline) in Antarctica; (b) bed
221 elevation of Totten Glacier, the red curve represents the grounding line.
222



223
224 **Figure 2.** The spatial distribution of the 8 GHF datasets for Totten Glacier (a–h) used
225 as input data in Huang et al. (2024). The purple line depicts the grounding line.
226

227 The spatial distribution of modelled basal temperature using the 8 GHFs displays
228 both similarities and heterogeneity. In the northern part of Totten Glacier, there is a
229 consistent warm-bedded pattern across all eight simulation results (Fig. S1), which
230 originates from the grounding line and extends upstream to approximately 71°S. This
231 warm-bedded area is not contiguous with the lateral boundaries of Totten Glacier but is
232 instead bordered by cold bed. All 8 GHF datasets produce low basal ice temperatures
233 in the inland southwest, with Purucker et al. (2012), Shapiro and Ritzwoller (2004),
234 Shen et al. (2020) and Lösing and Ebbing (2021) being colder. The basal ice velocities



235 modelled from the 8 different GHF datasets produce similar spatial distributions (Fig.
236 S2), which can be expected as they were derived using the same inverse method and
237 constrained by the identical observed surface ice velocity. The modelled basal ice
238 velocity is fast near the grounding line and its upstream area. There are also high
239 velocities between 70°S and 72°S close to the western boundary of Totten Glacier,
240 which are associated with subglacial canyon features in the basal topography (Fig. 1b)
241 and observed fast surface ice velocity there.

242

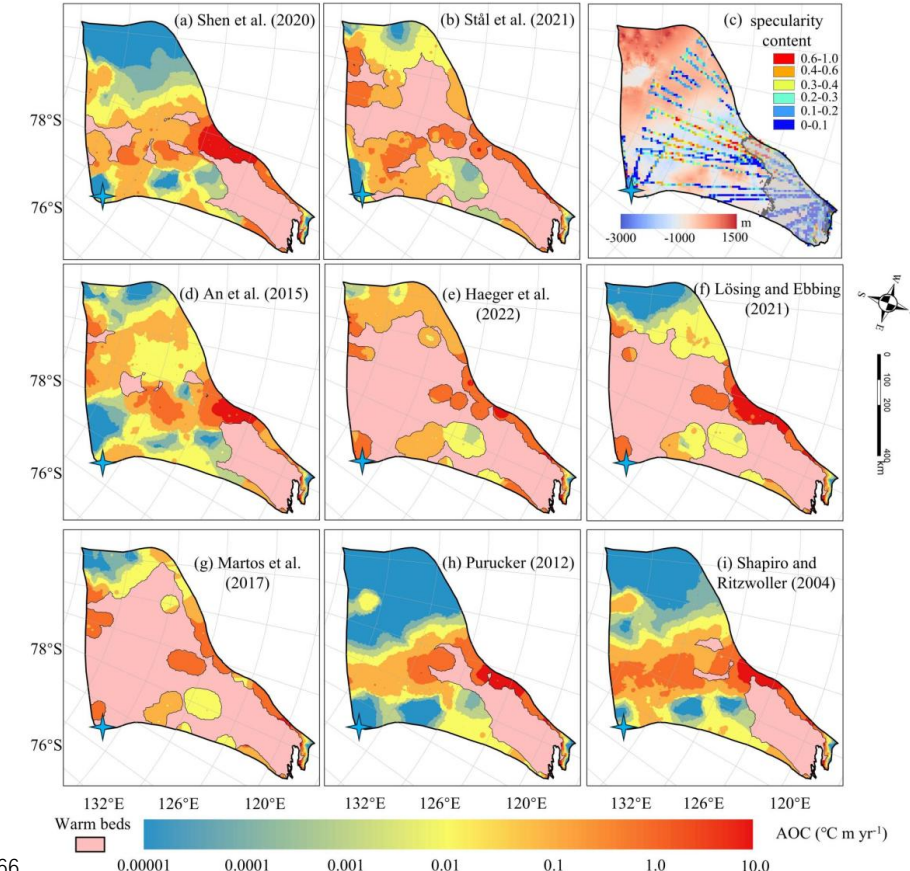
243 3.2 Spatial Distribution of Inconsistencies

244 We calculate the absolute inconsistencies, AOH , in the warm bed, and AOC in the
245 cold bed. The spatial distribution of AOC reveals that most GHF datasets exhibit
246 significant local overcooling inconsistencies at the subglacial canyon between 70°S and
247 72°S (Fig. 3). There is fast basal sliding in the inverse model results (Fig. S2), however,
248 the modelled basal ice temperatures inferred from most of the GHF datasets are below
249 the pressure melting point (Fig. S1). High specularity content in radar data (Fig. 3c)
250 suggests the presence of basal water in the subglacial canyons here (Dow et al., 2020;
251 Huang et al., 2024), which also suggests that the basal ice temperature should be at the
252 pressure melting point and confirms the inconsistency between the modelled
253 temperature and velocity fields.

254 The area near the grounding line is characterized by fast ice flow and warm bed
255 (Fig. 3), yet some of the margin is cold-bedded with modelled basal temperature below
256 the pressure melting point, resulting in high AOC . Overall, modelled results with most
257 GHF datasets show small overcooling inconsistencies. The modelled results using GHF
258 from Purucker et al. (2012), Shapiro and Ritzwoller (2004), Shen et al. (2020), Lösing
259 and Ebbing (2021) exhibit no overcooling inconsistency in southwestern Totten Glacier
260 (Fig. 3).

261 The spatial distribution of relative overcooling inconsistencies, ROC (Fig. 4),
262 differs from that of absolute inconsistencies, AOC , and is due to the spatial variability
263 in surface ice speed. The largest value of ROC across most GHF occurs at Dome C,
264 where the observed surface ice speed is close to zero.

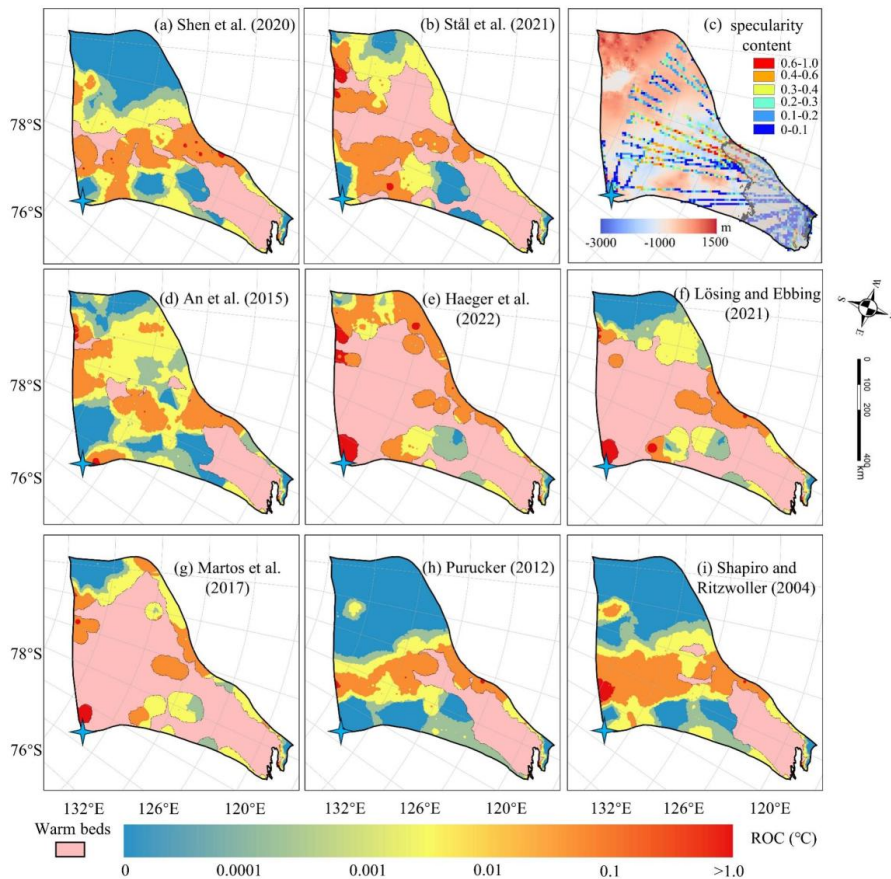
265



266

267 **Figure 3.** Spatial distribution of AOC inconsistency in modelled cold-bedded regions
268 (a-b, d-i) associated with the GHFs (a-h) in Fig. 2. The colormap is on logarithmic
269 scale. The pink region represents modelled warm bed. (c) Specularity content sourced
270 from radar data collected by ICECAP (Dow et al., 2020) with the bed elevation in the
271 background. Gray area in (c) corresponds to surface speed exceeding 30 m yr^{-1} . The
272 blue star represents Dome C.

273



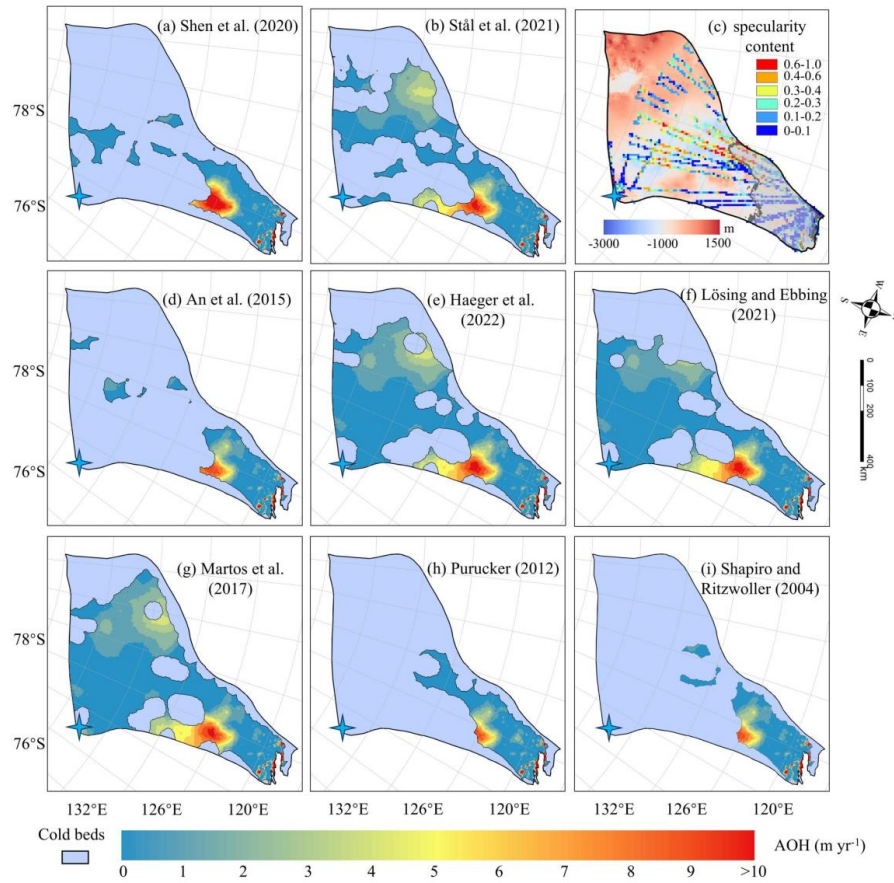
274
275 **Figure 4.** The spatial distribution of relative overcooling (ROC) inconsistency in cool
276 beds with (a), (b) and (d) to (i) corresponding to the GHFs (a – h) in Figure 2. The pink
277 area represents the warm beds. Dome C is marked by a blue star. (c) Locations of
278 specularity content derived from radar data collected by ICECAP (Dow et al., 2020)
279 and with the bed elevation in the background. The gray curve is the contour of the
280 surface speed of 30 m yr^{-1} . Note the colormap is non-linear.

281

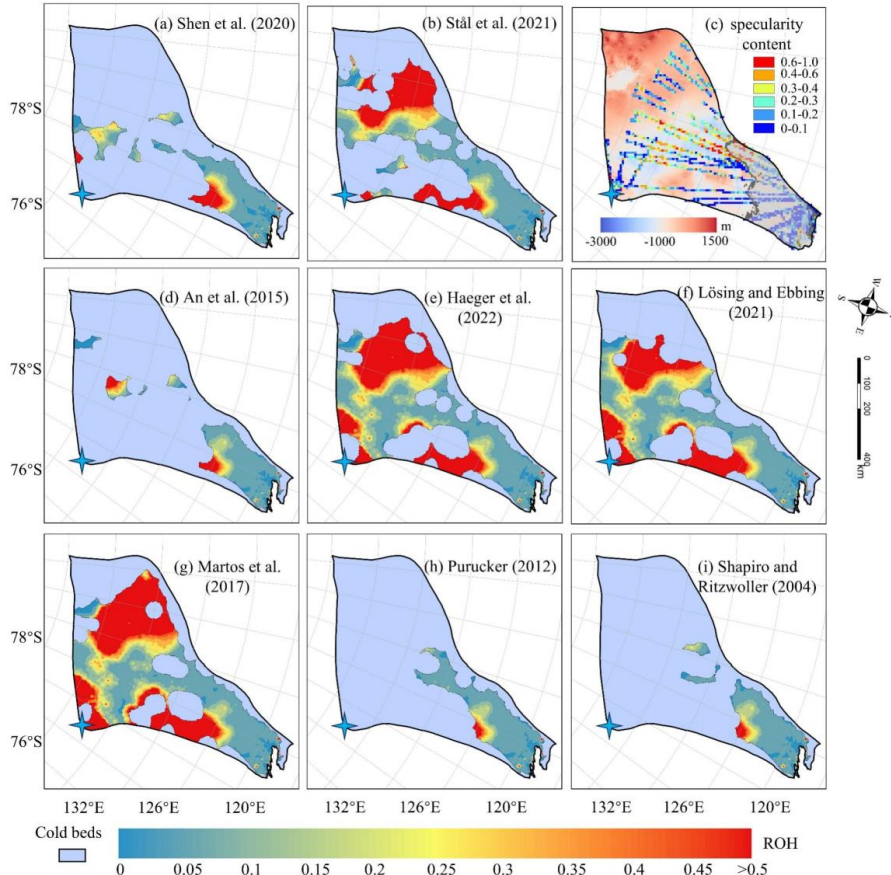
282 The GHF datasets of Stål et al. (2021), Haeger et al. (2022), Lösing and Ebbing
283 (2021) and Martos et al. (2017) which have higher than average GHF values provide
284 larger areas of warm bed than the other 4 GHFs. The simulations with all 8 GHFs yield
285 similar spatial distributions of AOH (Fig. 5) on the common area of warm bed, and
286 similar locations of high AOH values. A common high AOH area is located between
287 69°S and 72°S in the eastern part of Totten Glacier, due to simulated surface ice



288 velocities greatly exceeding the observed surface ice velocities. Low specularity
289 content from radar data (Fig. 5c) suggests there is no basal water in the area (Dow et
290 al., 2020; Huang et al., 2024). Therefore, it is likely that the basal ice temperature is
291 overestimated there. The simulations with all the 8 GHFs also yield similar spatial
292 distribution of ROH (Fig. 6), but its largest values are mostly in the slow flowing region
293 as one may expect from its formulation (Eq. (3)).



294 **Figure 5.** Spatial distribution of AOH in warm-bedded regions with **(a-b, d-i)**
295 corresponding to the GHFs **(a-h)** in Fig. 2. The blue region indicates cold-bedded areas.
296 **(c)** Locations of specularity content, same as Fig. 3c. The blue star represents Dome C.
297
298



299
300 **Figure 6.** The spatial distribution of relative overheating (ROH)
301 inconsistency in warm
302 beds with (a), (b) and (d) to (i) corresponding to the GHFs (a - h) in Figure 2. The light
303 purple mask represents the cold beds. (c) Locations of specularity content (coloured
304 points), same as Fig. 5.

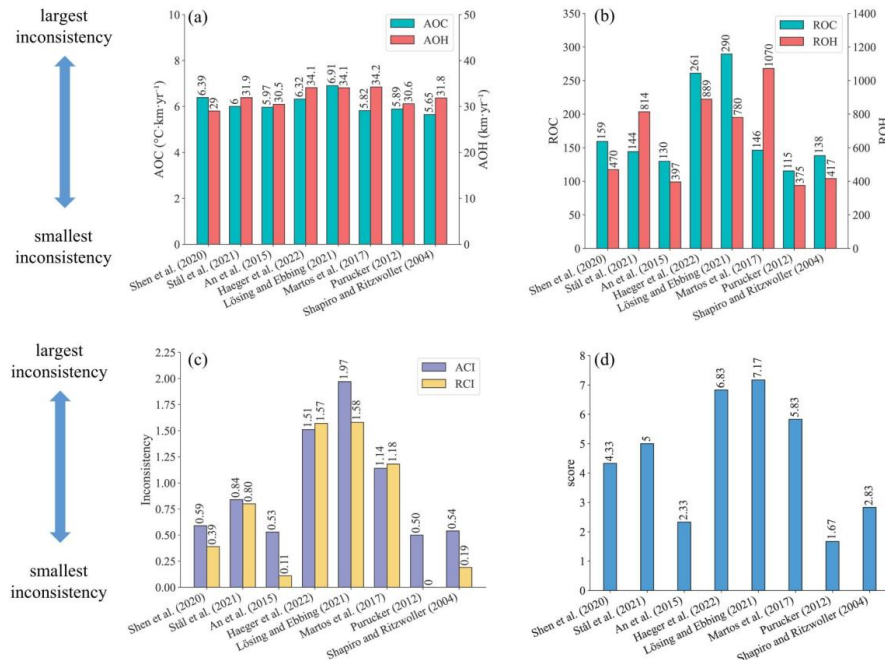
305 **3.3 Evaluation of Model Inconsistency with Eight GHFs**

306 All inconsistency indices for the simulation results using the eight GHF datasets
307 are illustrated in Fig. 7. The overheating inconsistency associated with Purucker et al.
308 (2012) and Shapiro and Ritzwoller (2004) GHFs is predominantly localized in fast-
309 flowing regions. Consequently, after normalization by the surface observed ice speed,
310 their relative rankings improve (Fig. 7). The GHFs from Purucker et al. (2012), An et
311 al. (2015), Shapiro and Ritzwoller (2004), and Shen et al. (2020) demonstrate balanced
312 performance with respect to both overheating and overcooling inconsistency metrics,



313 thereby securing the top four positions in both *ACI* and *RCI*. Their *ACI* values exhibit
314 similarity, ranging from 0.50 to 0.59 (Fig. 7c). In contrast, simulation result utilizing
315 Martos et al. (2017) GHF exhibits low *AOC* but high *AOH*. Simulation results utilizing
316 Stål et al. (2021) GHF show low *ROC* but relatively high *ROH*. Notably, simulation
317 results employing GHFs from Martos et al. (2017), Haeger et al. (2022), and Lösing
318 and Ebbing (2021) demonstrate comparably high *AOH* values. These four GHF
319 datasets—Martos et al. (2017), Stål et al. (2021), Haeger et al. (2022), and Lösing and
320 Ebbing (2021)—are ranked in the bottom four positions for both *ACI* and *RCI* metrics.
321 Furthermore, the ranking order of the eight GHFs remains consistent between *ACI* and
322 *RCI*.

323 We combine the above six metrics using the ranking of each metric from 1 to 8,
324 with 1 denoting the smallest inconsistency and 8 the largest. The final averaged ranking
325 (Fig. 7d) using the arithmetic mean of the individual metric scores, is the same as that
326 of *ACI* and *RCI*. Purucker et al. (2012), An et al. (2015) and Shapiro and Ritzwoller
327 (2004) GHFs occupy the top three positions. Following closely, Shen et al. (2020) and
328 Stål et al. (2021) GHFs secure the 4th and 5th positions, respectively. Martos et al.
329 (2017), Haeger et al. (2022) and Lösing and Ebbing (2021) GHFs are ranked as the
330 bottom three among the eight GHFs in Totten Glacier. The thermal state produced by
331 the optimal GHF result shows that warm beds predominantly cluster around the
332 grounding line and its upstream regions. Conversely, the inland areas of Totten largely
333 exhibit cold temperatures, with relatively sparse warm-bedded areas.



334

335 **Figure 7.** Six inconsistency indicators and the final ranking of 8 GHF datasets. **(a)** the
336 cumulative values of *AOC* across grid points over cold bed region and *AOH* across grid
337 points over warm bed region; **(b)** the cumulative values of *ROC* across grid points over
338 cold bed region and *ROH* across grid points over warm bed region; **(c)** the absolute and
339 relative combined inconsistencies, *ACI* and *RCI*; **(d)** the average of ranking scores from
340 1 to 8 using the six inconsistency indicators. The value of inconsistencies and scores
341 are labeled at the top of the bars.

342

343 4. Discussion

344 4.1 Causes of Inconsistencies and Sources of Uncertainty

345 Our method evaluates the quality of an ice sheet temperature field by quantifying
346 the inconsistency between that temperature field and the velocity field that is obtained
347 if that temperature field is used to compute the rheology in a mechanical inversion.
348 Because mechanical inversions use surface velocity observations as a constraint, we
349 have developed an indirect method for using surface velocity observations to check the
350 quality of an englacial temperature simulation. However, the mere fact that
351 inconsistencies exist does not by itself tell us what caused those inconsistencies.

352 Broadly speaking, the measured inconsistencies can come from two sources:
353 temperature or velocity. Uncertainties in any of the input datasets used to compute those



354 two fields can produce inconsistencies, as can simplifications in the model physics.
355 Here, we have tested the influence of one particular boundary condition, GHF, since
356 that field is particularly hard to constrain. Because all other inputs are kept constant,
357 the differences in the inconsistencies that we calculated between different simulations
358 can be attributed to the GHF fields. However, we also found that all of the models we
359 tested had non-zero inconsistency (Fig. 3; Fig. 5). The absolute inconsistencies, *AOH*
360 and *AOC*, had particularly small between-model variability in comparison to their mean
361 value. This could be because none of the input GHF fields correctly captured the true
362 GHF, but it could also indicate problems with other model inputs. For instance, the
363 surface temperature used in Huang et al. (2024) represents the present-day climate, but
364 the thermal structure of the ice sheet may reflect colder temperatures during the last
365 glacial cycle. We discuss an additional experiment we performed to test the influence
366 of uncertainty in surface temperature on our inconsistency metrics in Section 4.3 below.
367 By contrast, surface accumulation rate should have been lower during glacial periods,
368 which would have a warming influence on ice sheet temperatures. Uncertainties in bed
369 topography should influence both our thermal and our mechanical models, with deeper
370 ice being more likely to be warm, and with errors in ice thickness producing
371 compensating errors in basal sliding in our mechanical inversion. In the study of Huang
372 et al. (2024), BedMachine v2 was used for ice thickness and subglacial topography.
373 However, Bedmap3 (Pritchard et al., 2025) has better-resolved mountains and smoother
374 trough margins.

375 The simulation results we use from Huang et al. (2024) came from a 3D isotropic
376 full-Stokes ice flow model. While full-Stokes is generally considered the gold standard
377 of ice sheet mechanical modeling, the use of an isotropic rheology may not be valid in
378 some parts of the ice sheet, such as near ice divides or at the margin of an ice stream
379 where the history of past ice deformation creates anisotropic crystal fabric that affects
380 the present-day mechanical properties (Martín et al., 2009; Zhao et al., 2018b; Zwinger
381 et al., 2014). Isotropic flow laws often require the use of an “enhancement factor” for
382 vertical shear in the lower part of the ice column, an ad hoc correction that would have
383 a particularly large influence on our computed overcooling metrics. Thus the isotropic
384 flow law potentially introduces errors in modelled strain rates and, hence, bias in basal
385 sliding velocities obtained by inversion methods (Budd and Jacka, 1989; Gerber et al.,
386 2023; Rathmann and Lilien, 2022). Simulated surface ice velocities can be influenced
387 by other factors in addition to ice fabric; shear margins are also impacted by
388 accumulated rupture, such as damage along a shear margin (e.g., Benn et al., 2022;
389 Lhermitte et al., 2020; Schoof, 2004; Sun et al., 2017). Ice deposited during the last
390 glaciation has different chemistry (especially concentrations of chloride and possibly
391 sulphate ions) which leads to smaller crystals that develop a strong, near-vertical,
392 single-maximum fabric (Paterson, 1991). However, ice fabric data is sparse, known



393 from direct observations at ice cores (Azuma and Higashi, 1985) or inferred from
394 specialized radar measurements (Fujita and Mae, 1994; Jordan et al., 2022), and its
395 impact beyond the scope of this study as we refrain from incorporating additional
396 observational data relying only on widely-available surface ice velocities.

397 Our inconsistency metrics are designed to provide bidirectional constraints,
398 wherein the model is penalized for both overheating and overcooling. By adopting this
399 bidirectional constraint framework, we aim to mitigate the risk of unidirectional
400 constraints leading to excessively cold or warm outcomes being deemed optimal.
401 However, our inconsistency metrics only provide a bidirectional constraint when
402 viewed in a spatially integrated sense. Locally, we only have unidirectional constraints.
403 This is because our overheating metrics are only computed where the bed is at the
404 melting point, and our overcooling metrics are only computed where the bed is below
405 the melting point. This makes methodological sense, as we know for sure that sliding
406 must only occur where the bed is warm. However, in reality it is entirely possible that
407 some of the areas where the modelled bed reaches the pressure melting point are still
408 too cold (the modelled melt rate is lower than the real melt rate), and conversely, it is
409 also possible that some of the areas where the modelled bed is below the pressure
410 melting point are still too warm (the real temperature is colder still). Our method cannot
411 identify these areas. Thus, our inconsistency metrics may underestimate variability in
412 the ice sheet thermal state: we have no way to penalize cold regions that are not cold
413 enough or warm regions that are not warm enough. We leave the development of these
414 constraints to future work.

415

416 **4.2 Sensitivity of Inconsistencies to GHF Datasets**

417 Comparing the GHF dataset rankings between this study and Huang et al. (2024),
418 we find that the top 4 and the bottom 4 are the same in the two studies, albeit with slight
419 variations in ranking. The lower ranking of Shen et al. (2020) in this study may be
420 attributed to several factors. Firstly, Huang et al. (2024) excludes areas with ice speed
421 exceeding 30 m a^{-1} (Fig. 3c) because specularity content is an ambiguous indicator of
422 wet beds there. Secondly, the GHF from Shen et al. (2020) yields higher basal
423 temperature and also faster basal ice velocities in most of the cold bed of Totten Glacier,
424 hence exhibits greater overcooling inconsistency, compared with Purucker et al. (2012),
425 leading to a decrease in its rankings (Fig. S3). Lastly, Huang et al. (2024) primarily
426 relied on specularity content, while our study evaluated datasets based on
427 inconsistencies in the simulation results. Despite these methodological differences, both
428 studies identified four relatively well-performing GHF datasets for Totten Glacier,
429 which exhibit similar distributions of warm and cold beds when compared to the other
430 four datasets (Fig. 3 and Fig. 5). This similarity underscores that the warm bed is
431 concentrated near and upstream of the grounding line. Datasets from Stål et al. (2021),



432 Martos et al. (2017), Haeger et al. (2022), and Lösing and Ebbing (2021) exhibit a
433 tendency to overestimate GHF in central Totten Glacier.

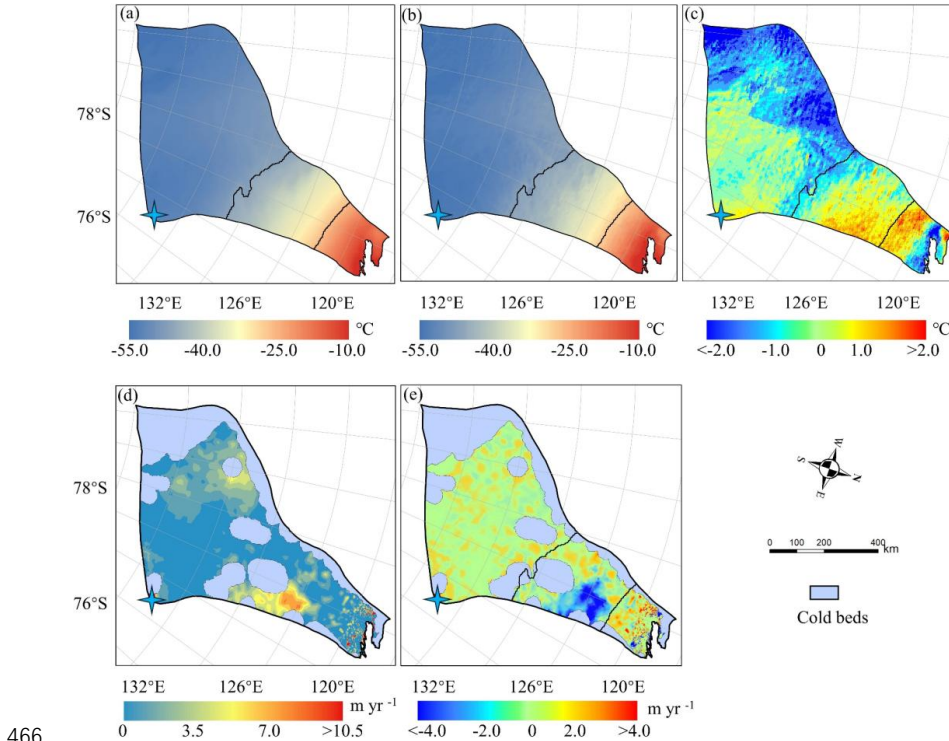
434 Simulations employing GHF datasets from Stål et al. (2021), Martos et al. (2017),
435 Haeger et al. (2022), and Lösing and Ebbing (2021) yield more extensive warm-bedded
436 regions and are expected to exhibit greater overheating inconsistency. Nevertheless,
437 these models also exhibit relatively high overcooling inconsistency despite the limited
438 extent of cold-bedded regions. We quantified the discrepancies between these four GHF
439 datasets and the Purucker et al. (2012) GHF in terms of modelled basal velocity, basal
440 temperature relative to the pressure melting point, and *AOC* (Fig. S4). The Purucker et
441 al. (2012) GHF yields lower basal ice temperatures and slower basal velocities across
442 most cold-bedded regions, consequently resulting in lower *AOC* values compared to
443 the other four GHF datasets.

444

445 **4.3 Implications for Ice Sheet Dynamics**

446 There is a common area between 69°S and 72°S in the eastern part of Totten
447 Glacier with the largest *AOH* (Fig. 5) for all the GHFs varying from 48 to 70 mW m⁻²,
448 which suggests that the *AOH* inconsistency is from other ice sheet properties rather than
449 GHF. Zhang et al. (2022) reconstructed Antarctic near-surface air temperature based on
450 MODIS land surface temperature measurements and in situ air temperature records
451 from meteorological stations from 2001 to 2018. We compared the reconstruction of
452 near-surface air temperature in the year 2001 (Zhang et al., 2022) and the ALBMAP v1
453 dataset used in Huang et al. (2024). The surface air temperature in the area with large
454 *AOH* from ALBMAP v1 is 0.6-3.1 °C higher than that from the reconstructed near-
455 surface air temperature in 2001 (Fig. 8). The MODIS-based near-surface air
456 temperature product shows warming in Totten Glacier from 2001 to 2018. Even so, the
457 surface air temperature in the area with large *AOH* from ALBMAP v1 is still higher
458 than that in 2018 but over a smaller area. Therefore, we infer that the large *AOH* may
459 be attributed to the present-day ice surface temperature derived from ALBMAP v1 in
460 this area being unrealistically warm. The englacial temperature will be lower than
461 present-day ice sheet surface temperature used in the model but warmer than the
462 average surface temperature during the last glacial-interglacial cycle. We lowered the
463 surface ice temperature in this area by 1 °C, reran the simulation, and found that *AOH*
464 with all the GHFs was halved (Fig. 8e).

465



466 **Figure 8.** Surface ice temperature from ALBMAP v1 (a) and MODIS-based near-
467 surface air temperature (b) in the year 2001, and their difference (c). (d) The AOH using
468 modified surface ice temperature by reducing the temperature between the two thick
469 black curves (contour lines of -44°C and -26°C) in (a) by 1°C and GHF of Martos
470 et al. (2017). (e) The difference between the AOH using cooler surface ice temperature
471 and the original AOH. The blue star represents Dome C.

473

474 Given that data assimilation and inverse methods are widely employed to infer
475 basal friction coefficients in ice sheet simulations, it is essential to acknowledge the
476 impact of the inconsistencies identified in our study on ice sheet dynamics. A cold bed
477 is supposed to provide substantial resistance and limit basal sliding; however, if the
478 basal temperature is overestimated, it may decrease viscosity and enhance basal sliding.
479 This overheating inconsistency would lead to an overestimation of ice flow speeds,
480 discharge, and the dynamic ice loss (Artemieva, 2022; Burton-Johnson et al., 2020).
481 Similarly, under representation of warm bedding would slow ice discharge estimates,
482 and hence potential ice sheet response to climate warming. The basal thermal regime



483 critically influences the stability of grounding lines and the behavior of ice streams. In
484 a warming climate, increases in geothermal or frictional heating can trigger basal
485 thawing in these areas, lowering basal friction and potentially initiating rapid grounding
486 line retreat—a key component of marine ice sheet instability (MISI) (Reese et al., 2023;
487 Ross et al., 2012). Without incorporating a self-consistent thermal model into the
488 inversion, projections may misrepresent the onset and extent of these dynamic
489 instabilities. Our findings underscore that a fully coupled inversion framework would
490 use not only surface velocity data but also incorporate direct or proxy observations of
491 basal temperature and subglacial hydrology. Such an approach would better constrain
492 the basal friction coefficient in a physically consistent manner, reducing the risk of
493 producing nonphysical states. This integration is especially critical for projections of
494 ice sheet evolution under climate change, as the dynamic response is sensitive to even
495 small changes in basal conditions.

496

497 5. Conclusion

498 We propose a novel and rapid method to quantify the inconsistencies between
499 modelled basal ice temperature and observed surface ice speed and assess the quality
500 of ice sheet model simulation results without using subglacial observation data.
501 Previously, it has been assumed that checking the quality of an ice sheet temperature
502 model required in situ observations, whether from ice cores or geophysical techniques
503 like ice penetrating radar. By using the ice temperature field to compute the rheology
504 structure needed for a mechanical inversion and then quantifying the inconsistency
505 between the inverted velocity field and the original ice temperature field, we are able
506 to use remotely sensed surface velocity observations as a check on the quality of
507 modelled englacial temperatures. Given the challenges in acquiring subglacial data, our
508 method can provide a streamlined and effective approach to evaluation.

509 We apply this method to the simulation results of Totten Glacier using a 3D full-
510 Stokes model with 8 different GHF datasets. Assuming the inconsistencies are mainly
511 due to unrealistic GHF datasets, we use the inconsistencies to assess the reliability of
512 those GHF datasets. We compare our GHF ranking with that by Huang et al. (2024)
513 which used specularity content to derive a two-sided constraint on the basal thermal
514 state. We find that the top 4 and the bottom 4 GHFs are the same in the two studies,
515 albeit with slight variations in ranking. Furthermore, we find that the simulations with
516 all GHF datasets underestimate the basal ice temperature in a canyon on the western
517 boundary of Totten Glacier, and we infer that the common high overheating
518 inconsistencies with all the GHF datasets in the eastern Totten Glacier between 69°S
519 and 72°S may be attributed to the unrealistically warm surface ice temperature used
520 there in the model. While we demonstrate that this approach works on simulation results
521 for Totten Glacier, testing of the method on other glaciers would be useful to assess if



522 the approach is worthwhile for revealing ambiguous conflicts in observations and
523 simulations.

524

525

526

527 *Data availability.* MEaSUREs BedMachine Antarctica, version 2, is available at
528 <https://doi.org/10.5067/E1QL9HFQ7A8M> (Morlighem, 2020). MEaSUREs InSAR-
529 Based Antarctic Ice Velocity Map, version 2, is available at
530 <https://doi.org/10.5067/D7GK8F5J8M8R> (Rignot et al., 2017). MEaSUREs Antarctic
531 Boundaries for IPY 2007–2009 from Satellite Radar, version 2, is available at
532 <https://doi.org/10.5067/AXE4121732AD> (Mouginot et al., 2017). ALBMAP v1 and the
533 GHF dataset of Shapiro and Ritzwoller (2004) are available at
534 <https://doi.org/10.1594/PANGAEA.734145> (Le Brocq et al., 2010b). The GHF dataset
535 of An et al. (2015) is available at
536 <http://www.seismolab.org/model/antarctica/lithosphere/AN1-HF.tar.gz> (last access: 11
537 April 2023). The GHF dataset of Shen et al. (2020) is available at
538 <https://sites.google.com/view/weisen/research-products?authuser=0> (last access: 11
539 April 2023). The GHF dataset of Martos (2017) is available at
540 <https://doi.org/10.1594/PANGAEA.882503>. The GHF dataset of Purucker (2012) is
541 available
542 https://core2.gsfc.nasa.gov/research/purucker/heatflux_mf7_foxmaule05.txt (last
543 access: 11 April 2023).

544

545 *Author contributions.* LZ and JCM conceived the study. LZ, MW, and JCM designed
546 the methodology. JW and LZ analyzed the data and conducted visualization. JW
547 and LZ wrote the original draft, and all the authors revised the paper.

548

549 *Competing interests.* The contact author has declared that none of the authors has any
550 competing interests.

551

552 *Acknowledgements.* This work was supported by National Key Research and
553 Development Program of China (grant no. 2021YFB3900105) and Academy of
554 Finland (grant no. 355572).

555 **References**

556 Albrecht, T., Winkelmann, R., and Levermann, A.: Glacial-cycle simulations of the Antarctic Ice
557 Sheet with the Parallel Ice Sheet Model (PISM) – Part 1: Boundary conditions and climatic
558 forcing, *The Cryosphere*, 14, 599–632, <https://doi.org/10.5194/tc-14-599-2020>, 2020.

559 An, M., Wiens, D. A., Zhao, Y., Feng, M., Nyblade, A., Kanao, M., Li, Y., Maggi, A., and Lévêque,
560 J.: Temperature, lithosphere-asthenosphere boundary, and heat flux beneath the Antarctic Plate
561 inferred from seismic velocities, *J. Geophys. Res. Solid Earth*, 120, 8720–8742,



562 <https://doi.org/10.1002/2015JB011917>, 2015.

563 Artemieva, I. M.: Antarctica ice sheet basal melting enhanced by high mantle heat, *Earth-Sci. Rev.*,
564 226, 103954, <https://doi.org/10.1016/j.earscirev.2022.103954>, 2022.

565 Azuma, N. and Higashi, A.: Formation Processes of Ice Fabric Pattern in Ice Sheets, *Ann. Glaciol.*,
566 6, 130–134, <https://doi.org/10.3189/1985AoG6-1-130-134>, 1985.

567 Benn, D. I., Luckman, A., Åström, J. A., Crawford, A. J., Cornford, S. L., Bevan, S. L., Zwinger, T.,
568 Gladstone, R., Alley, K., Pettit, E., and Bassist, J.: Rapid fragmentation of Thwaites Eastern Ice
569 Shelf, *The Cryosphere*, 16, 2545–2564, <https://doi.org/10.5194/tc-16-2545-2022>, 2022.

570 Brondex, J., Gagliardini, O., Gillet-Chaulet, F., and Durand, G.: Sensitivity of grounding line
571 dynamics to the choice of the friction law, *J. Glaciol.*, 63, 854–866,
572 <https://doi.org/10.1017/jog.2017.51>, 2017.

573 Brondex, J., Gillet-Chaulet, F., and Gagliardini, O.: Sensitivity of centennial mass loss projections
574 of the Amundsen basin to the friction law, *The Cryosphere*, 13, 177–195,
575 <https://doi.org/10.5194/tc-13-177-2019>, 2019.

576 Budd, W. F. and Jacka, T. H.: A review of ice rheology for ice sheet modelling, *Cold Reg. Sci.
577 Technol.*, 16, 107–144, [https://doi.org/10.1016/0165-232X\(89\)90014-1](https://doi.org/10.1016/0165-232X(89)90014-1), 1989.

578 Budd, W. F., Keage, P. L., and Blundy, N. A.: Empirical Studies of Ice Sliding, *J. Glaciol.*, 23, 157–
579 170, <https://doi.org/10.3189/S0022143000029804>, 1979.

580 Burton-Johnson, A., Dziadek, R., and Martin, C.: Review article: Geothermal heat flow in
581 Antarctica: current and future directions, *The Cryosphere*, 14, 3843–3873,
582 <https://doi.org/10.5194/tc-14-3843-2020>, 2020.

583 Choi, Y., Seroussi, H., Morlighem, M., Schlegel, N.-J., and Gardner, A.: Impact of time-dependent
584 data assimilation on ice flow model initialization and projections: a case study of Kjer Glacier,
585 Greenland, *The Cryosphere*, 17, 5499–5517, <https://doi.org/10.5194/tc-17-5499-2023>, 2023.

586 Cornford, S. L., Martin, D. F., Payne, A. J., Ng, E. G., Le Brocq, A. M., Gladstone, R. M., Edwards,
587 T. L., Shannon, S. R., Agosta, C., Van Den Broeke, M. R., Hellmer, H. H., Krinner, G.,
588 Ligtenberg, S. R. M., Timmermann, R., and Vaughan, D. G.: Century-scale simulations of the
589 response of the West Antarctic Ice Sheet to a warming climate, *The Cryosphere*, 9, 1579–1600,
590 <https://doi.org/10.5194/tc-9-1579-2015>, 2015.

591 Dow, C. F., McCormack, F. S., Young, D. A., Greenbaum, J. S., Roberts, J. L., and Blankenship, D.
592 D.: Totten Glacier subglacial hydrology determined from geophysics and modeling, *Earth
593 Planet. Sci. Lett.*, 531, 115961, <https://doi.org/10.1016/j.epsl.2019.115961>, 2020.

594 Dziadek, R., Gohl, K., Diehl, A., and Kaul, N.: Geothermal heat flux in the Amundsen Sea sector
595 of West Antarctica: New insights from temperature measurements, depth to the bottom of the
596 magnetic source estimation, and thermal modeling, *Geochem. Geophys. Geosystems*, 18,
597 2657–2672, <https://doi.org/10.1002/2016GC006755>, 2017.

598 Fisher, A. T., Mankoff, K. D., Tulaczyk, S. M., Tyler, S. W., and Foley, N.: High geothermal heat
599 flux measured below the West Antarctic Ice Sheet, *Sci. Adv.*, 1(6), e1500093,
600 <https://doi.org/10.1126/sciadv.1500093>, 2015.

601 Fowler, A. C.: A theoretical treatment of the sliding of glaciers in the absence of cavitation, *Philos.*



602 Trans. R. Soc. Lond. Ser. Math. Phys. Sci., 298, 637–681,
603 <https://doi.org/10.1098/rsta.1981.0003>, 1981.

604 Fujita, S. and Mae, S.: Strain in the ice sheet deduced from the crystal-orientation fabrics from bare
605 icefields adjacent to the Sør-Rondane Mountains, Dronning Maud Land, East Antarctica, *J.
606 Glaciol.*, 40, 135–139, <https://doi.org/10.3189/S002214300003907>, 1994.

607 Gagliardini, O., Cohen, D., Råback, P., and Zwinger, T.: Finite-element modeling of subglacial
608 cavities and related friction law, *J. Geophys. Res. Earth Surf.*, 112, F02027,
609 <https://doi.org/10.1029/2006JF000576>, 2007.

610 Gerber, T. A., Lilien, D. A., Rathmann, N. M., Franke, S., Young, T. J., Valero-Delgado, F., Ershadi,
611 M. R., Drews, R., Zeising, O., Humbert, A., Stoll, N., Weikusat, I., Grinsted, A., Hvidberg, C.
612 S., Jansen, D., Miller, H., Helm, V., Steinhage, D., O'Neill, C., Paden, J., Gogineni, S. P., Dahl-
613 Jensen, D., and Eisen, O.: Crystal orientation fabric anisotropy causes directional hardening of
614 the Northeast Greenland Ice Stream, *Nat. Commun.*, 14, 2653, <https://doi.org/10.1038/s41467-023-38139-8>, 2023.

615 Gillet-Chaulet, F., Gagliardini, O., Seddik, H., Nodet, M., Durand, G., Ritz, C., Zwinger, T., Greve,
616 R., and Vaughan, D. G.: Greenland ice sheet contribution to sea-level rise from a new-
617 generation ice-sheet model, *The Cryosphere*, 6, 1561–1576, <https://doi.org/10.5194/tc-6-1561-2012>, 2012.

618 Gladstone, R., Schäfer, M., Zwinger, T., Gong, Y., Strozzi, T., Mottram, R., Boberg, F., and Moore,
619 J. C.: Importance of basal processes in simulations of a surging Svalbard outlet glacier, *The
620 Cryosphere*, 8, 1393–1405, <https://doi.org/10.5194/tc-8-1393-2014>, 2014.

621 Greenbaum, J. S., Blankenship, D. D., Young, D. A., Richter, T. G., Roberts, J. L., Aitken, A. R. A.,
622 Legresy, B., Schroeder, D. M., Warner, R. C., van Ommen, T. D., and Siegert, M. J.: Ocean
623 access to a cavity beneath Totten Glacier in East Antarctica, *Nat. Geosci.*, 8, 294–298,
624 <https://doi.org/10.1038/ngeo2388>, 2015.

625 Haeger, C., Petrunin, A. G., and Kaban, M. K.: Geothermal Heat Flow and Thermal Structure of the
626 Antarctic Lithosphere, *Geochem. Geophys. Geosystems*, 23, e2022GC010501,
627 <https://doi.org/10.1029/2022GC010501>, 2022.

628 Huang, Y., Zhao, L., Wolovick, M., Ma, Y., and Moore, J. C.: Using specularity content to evaluate
629 eight geothermal heat flow maps of Totten Glacier, *The Cryosphere*, 18, 103–119,
630 <https://doi.org/10.5194/tc-18-103-2024>, 2024.

631 Jordan, T. M., Martín, C., Brisbourne, A. M., Schroeder, D. M., and Smith, A. M.: Radar
632 Characterization of Ice Crystal Orientation Fabric and Anisotropic Viscosity Within an
633 Antarctic Ice Stream, *J. Geophys. Res. Earth Surf.*, 127, e2022JF006673,
634 <https://doi.org/10.1029/2022JF006673>, 2022.

635 Kamb, B.: Sliding motion of glaciers: Theory and observation, *Rev. Geophys.*, 8, 673–728,
636 <https://doi.org/10.1029/RG008i004p00673>, 1970.

637 Kang, H., Zhao, L., Wolovick, M., and Moore, J. C.: Evaluation of six geothermal heat flux maps
638 for the Antarctic Lambert–Amery glacial system, *The Cryosphere*, 16, 3619–3633,
639 <https://doi.org/10.5194/tc-16-3619-2022>, 2022.



642 Kim, B.-H., Seo, K.-W., Lee, C.-K., Kim, J.-S., Lee, W. S., Jin, E. K., and Van Den Broeke, M.:
643 Partitioning the drivers of Antarctic glacier mass balance (2003–2020) using satellite
644 observations and a regional climate model, *Proc. Natl. Acad. Sci.*, 121, e2322622121,
645 <https://doi.org/10.1073/pnas.2322622121>, 2024.

646 Larour, E., Seroussi, H., Morlighem, M., and Rignot, E.: Continental scale, high order, high spatial
647 resolution, ice sheet modeling using the Ice Sheet System Model (ISSM), *J. Geophys. Res.*,
648 117, F01022, <https://doi.org/10.1029/2011JF002140>, 2012.

649 Le Brocq, A. M., Payne, A. J., and Vieli, A.: An improved Antarctic dataset for high resolution
650 numerical ice sheet models (ALBMAP v1), *Earth Syst. Sci. Data*, 2, 247–260,
651 <https://doi.org/10.5194/essd-2-247-2010>, 2010.

652 Lipscomb, W. H., Leguy, G. R., Jourdain, N. C., Asay-Davis, X., Seroussi, H., and Nowicki, S.:
653 ISMIP6-based projections of ocean-forced Antarctic Ice Sheet evolution using the
654 Community Ice Sheet Model, *The Cryosphere*, 15, 633–661, <https://doi.org/10.5194/tc-15-633-2021>, 2021.

655 Lhermitte, S., Sun, S., Shuman, C., Wouters, B., Pattyn, F., Wuite, J., Berthier, E., and Nagler, T.:
656 Damage accelerates ice shelf instability and mass loss in Amundsen Sea Embayment, *Proc.
657 Natl. Acad. Sci.*, 117, 24735–24741, <https://doi.org/10.1073/pnas.1912890117>, 2020.

658 Lösing, M. and Ebbing, J.: Predicting Geothermal Heat Flow in Antarctica With a Machine Learning
659 Approach, *J. Geophys. Res. Solid Earth*, 126, e2020JB021499,
660 <https://doi.org/10.1029/2020JB021499>, 2021.

661 MacAyeal, D. R.: A tutorial on the use of control methods in ice-sheet modeling, *J. Glaciol.*, 39, 91–
662 98, <https://doi.org/10.3189/S0022143000015744>, 1993.

663 Martín, C., Gudmundsson, G. H., Pritchard, H. D., and Gagliardini, O.: On the effects of anisotropic
664 rheology on ice flow, internal structure, and the age-depth relationship at ice divides, *J.
665 Geophys. Res. Earth Surf.*, 114, F04001, <https://doi.org/10.1029/2008JF001204>, 2009.

666 Martos, Y. M., Catalán, M., Jordan, T. A., Golynsky, A., Golynsky, D., Eagles, G., and Vaughan, D.
667 G.: Heat Flux Distribution of Antarctica Unveiled, *Geophys. Res. Lett.*, 44, 11,417–11,426,
668 <https://doi.org/10.1002/2017GL075609>, 2017.

669 Maule, C. F., Purucker, M. E., Olsen, N., and Mosegaard, K.: Heat Flux Anomalies in Antarctica
670 Revealed by Satellite Magnetic Data, *Science*, 309, 464–467,
671 <https://doi.org/10.1126/science.1106888>, 2005.

672 McCormack, F. S., Roberts, J. L., Dow, C. F., Stål, T., Halpin, J. A., Reading, A. M., and Siegert, M.
673 J.: Fine-Scale Geothermal Heat Flow in Antarctica Can Increase Simulated Subglacial Melt
674 Estimates, *Geophys. Res. Lett.*, 49, e2022GL098539, <https://doi.org/10.1029/2022GL098539>,
675 2022.

676 Morlighem, M., Seroussi, H., Larour, E., and Rignot, E.: Inversion of basal friction in Antarctica
677 using exact and incomplete adjoints of a higher-order model, *J. Geophys. Res. Earth Surf.*, 118,
678 1746–1753, <https://doi.org/10.1002/jgrf.20125>, 2013.

679 Morlighem, M., Rignot, E., Binder, T., Blankenship, D., Drews, R., Eagles, G., Eisen, O., Ferraccioli,
680 F., Forsberg, R., Fretwell, P., Goel, V., Greenbaum, J. S., Gudmundsson, H., Guo, J., Helm, V.,



682 Hofstede, C., Howat, I., Humbert, A., Jokat, W., Karlsson, N. B., Lee, W. S., Matsuoka, K.,
683 Millan, R., Mouginot, J., Paden, J., Pattyn, F., Roberts, J., Rosier, S., Ruppel, A., Seroussi, H.,
684 Smith, E. C., Steinhage, D., Sun, B., Broeke, M. R. V. D., Ommen, T. D. V., Wessem, M. V.,
685 and Young, D. A.: Deep glacial troughs and stabilizing ridges unveiled beneath the margins of
686 the Antarctic ice sheet, *Nat. Geosci.*, 13, 132–137, <https://doi.org/10.1038/s41561-019-0510-8>, 2020.

688 Nye, J. F.: Glacier sliding without cavitation in a linear viscous approximation, *Proc. R. Soc. Lond.*
689 *Math. Phys. Sci.*, 315, 381–403, <https://doi.org/10.1098/rspa.1970.0050>, 1970.

690 Park, I.-W., Jin, E. K., Morlighem, M., and Lee, K.-K.: Impact of boundary conditions on the
691 modeled thermal regime of the Antarctic ice sheet, *The Cryosphere*, 18, 1139–1155,
692 <https://doi.org/10.5194/tc-18-1139-2024>, 2024.

693 Paterson, W. S. B.: Why ice-age ice is sometimes “soft,” *Cold Reg. Sci. Technol.*, 20, 75–98,
694 [https://doi.org/10.1016/0165-232X\(91\)90058-O](https://doi.org/10.1016/0165-232X(91)90058-O), 1991.

695 Pattyn, F.: Sea-level response to melting of Antarctic ice shelves on multi-centennial timescales
696 with the fast Elementary Thermomechanical Ice Sheet model (f.ETISh v1.0), *The*
697 *Cryosphere*, 11, 1851–1878, <https://doi.org/10.5194/tc-11-1851-2017>, 2017.

698 Payne, A. J., Nowicki, S., Abe-Ouchi, A., Agosta, C., Alexander, P., Albrecht, T., Asay-Davis, X.,
699 Aschwanden, A., Barthel, A., Bracegirdle, T. J., Calov, R., Chambers, C., Choi, Y., Cullather,
700 R., Cuzzone, J., Dumas, C., Edwards, T. L., Felikson, D., Fettweis, X., Galton-Fenzi, B. K.,
701 Goelzer, H., Gladstone, R., Golledge, N. R., Gregory, J. M., Greve, R., Hattermann, T.,
702 Hoffman, M. J., Humbert, A., Huybrechts, P., Jourdain, N. C., Kleiner, T., Munneke, P. K.,
703 Larour, E., Le Clec'H, S., Lee, V., Leguy, G., Lipscomb, W. H., Little, C. M., Lowry, D. P.,
704 Morlighem, M., Nias, I., Pattyn, F., Pelle, T., Price, S. F., Quiquet, A., Reese, R., Rückamp, M.,
705 Schlegel, N., Seroussi, H., Shepherd, A., Simon, E., Slater, D., Smith, R. S., Straneo, F., Sun,
706 S., Tarasov, L., Trusel, L. D., Van Breedam, J., Van De Wal, R., Van Den Broeke, M.,
707 Winkelmann, R., Zhao, C., Zhang, T., and Zwinger, T.: Future Sea Level Change Under
708 Coupled Model Intercomparison Project Phase 5 and Phase 6 Scenarios From the Greenland
709 and Antarctic Ice Sheets, *Geophys. Res. Lett.*, 48, e2020GL091741,
710 <https://doi.org/10.1029/2020GL091741>, 2021.

711 Peyaud, V., Bouchayer, C., Gagliardini, O., Vincent, C., Gillet-Chalet, F., Six, D., and Laarman,
712 O.: Numerical modeling of the dynamics of the Mer de Glace glacier, French Alps: comparison
713 with past observations and forecasting of near-future evolution, *The Cryosphere*, 14, 3979–
714 3994, <https://doi.org/10.5194/tc-14-3979-2020>, 2020.

715 Pittard, M. L., Roberts, J. L., Galton-Fenzi, B. K., and Watson, C. S.: Sensitivity of the Lambert-
716 Amery glacial system to geothermal heat flux, *Ann. Glaciol.*, 57, 56–68,
717 <https://doi.org/10.1017/aog.2016.26>, 2016.

718 Pollard, D. and DeConto, R. M.: A simple inverse method for the distribution of basal sliding
719 coefficients under ice sheets, applied to Antarctica, *The Cryosphere*, 6, 953–971,
720 <https://doi.org/10.5194/tc-6-953-2012>, 2012.

721 Pritchard, H. D., Arthern, R. J., Vaughan, D. G., and Edwards, L. A.: Extensive dynamic thinning



722 on the margins of the Greenland and Antarctic ice sheets, *Nature*, 461, 971–975,
723 <https://doi.org/10.1038/nature08471>, 2009.

724 Pritchard, H.D., Fretwell, P.T., Freymond, A.C. et al. Bedmap3 updated ice bed, surface and thickness
725 gridded datasets for Antarctica. *Sci Data* 12, 414 (2025). <https://doi.org/10.1038/s41597-025-04672-y>

726 Purucker, M.: Geothermal heat flux data set based on low resolution observations collected by the
727 CHAMP satellite between 2000 and 2010, and produced from the MF-6 model following the
728 technique described in Fox Maule et al. (2005), Interactive System for Ice sheet Simulation
729 [data set], https://core2.gsfc.nasa.gov/research/purucker/heatflux_mf7_foxmaule05.txt (last
730 access: 24 December 2023), 2012.

731 Rathmann, N. M. and Lilien, D. A.: Inferred basal friction and mass flux affected by crystal-
732 orientation fabrics, *J. Glaciol.*, 68, 236–252, <https://doi.org/10.1017/jog.2021.88>, 2022.

733 Reading, A. M.: Antarctic geothermal heat flow and its implications for tectonics and ice sheets,
734 *Nat. Rev. Earth Environ.*, 3, 814–831, <https://doi.org/10.1038/s43017-022-00348-y>, 2022.

735 Reese, R., Garbe, J., Hill, E. A., Urruty, B., Naughten, K. A., Gagliardini, O., Durand, G., Gillet-
736 Chaulet, F., Gudmundsson, G. H., Chandler, D., Langebroek, P. M., and Winkelmann, R.: The
737 stability of present-day Antarctic grounding lines – Part 2: Onset of irreversible retreat of
738 Amundsen Sea glaciers under current climate on centennial timescales cannot be excluded,
739 *The Cryosphere*, 17, 3761–3783, <https://doi.org/10.5194/tc-17-3761-2023>, 2023.

740 Ross, N., Bingham, R. G., Corr, H. F. J., Ferraccioli, F., Jordan, T. A., Le Brocq, A., Rippin, D. M.,
741 Young, D., Blankenship, D. D., and Siegert, M. J.: Steep reverse bed slope at the grounding
742 line of the Weddell Sea sector in West Antarctica, *Nat. Geosci.*, 5, 393–396,
743 <https://doi.org/10.1038/ngeo1468>, 2012.

744 Rignot, E., Mouginot, J., and Scheuchl, B.: MEaSUREs InSAR-Based Antarctica Ice Velocity Map,
745 Version 2, Boulder, Colorado USA, NASA National Snow and Ice Data Center Distributed
746 Active Archive Center [data Set], <https://doi.org/10.5067/D7GK8F5J8M8R>, 2017.

747 Rignot, E., Mouginot, J., Scheuchl, B., Van Den Broeke, M., Van Wessem, M. J., and Morlighem,
748 M.: Four decades of Antarctic Ice Sheet mass balance from 1979–2017, *Proc. Natl. Acad. Sci.*,
749 116, 1095–1103, <https://doi.org/10.1073/pnas.1812883116>, 2019.

750 Schannwell, C., Drews, R., Ehlers, T. A., Eisen, O., Mayer, C., Malinen, M., Smith, E. C., and
751 Eisermann, H.: Quantifying the effect of ocean bed properties on ice sheet geometry over 40
752 000 years with a full-Stokes model, *The Cryosphere*, 14, 3917–3934,
753 <https://doi.org/10.5194/tc-14-3917-2020>, 2020.

754 Schoof, C.: On the mechanics of ice-stream shear margins, *J. Glaciol.*, 50, 208–218,
755 <https://doi.org/10.3189/172756504781830024>, 2004.

756 Schoof, C.: The effect of cavitation on glacier sliding, *Proc. R. Soc. Math. Phys. Eng. Sci.*, 461,
757 609–627, <https://doi.org/10.1098/rspa.2004.1350>, 2005.

758 Schroeder, D. M., Blankenship, D. D., and Young, D. A.: Evidence for a water system transition
759 beneath Thwaites Glacier, West Antarctica, *Proc. Natl. Acad. Sci.*, 110, 12225–12228,
760 <https://doi.org/10.1073/pnas.1302828110>, 2013.

761



762 Schroeder, D. M., Blankenship, D. D., Raney, R. K., and Grima, C.: Estimating Subglacial Water
763 Geometry Using Radar Bed Echo Specularity: Application to Thwaites Glacier, West
764 Antarctica, *IEEE Geosci. Remote Sens. Lett.*, 12, 443–447,
765 <https://doi.org/10.1109/LGRS.2014.2337878>, 2015.

766 Seroussi, H., Nowicki, S., Simon, E., Abe-Ouchi, A., Albrecht, T., Brondex, J., Cornford, S., Dumas,
767 C., Gillet-Chaulet, F., Goelzer, H., Golledge, N. R., Gregory, J. M., Greve, R., Hoffman, M. J.,
768 Humbert, A., Huybrechts, P., Kleiner, T., Larour, E., Leguy, G., Lipscomb, W. H., Lowry, D.,
769 Mengel, M., Morlighem, M., Pattyn, F., Payne, A. J., Pollard, D., Price, S. F., Quiquet, A.,
770 Reerink, T. J., Reese, R., Rodehacke, C. B., Schlegel, N.-J., Shepherd, A., Sun, S., Sutter, J.,
771 Van Breedam, J., Van De Wal, R. S. W., Winkelmann, R., and Zhang, T.: initMIP-Antarctica:
772 an ice sheet model initialization experiment of ISMIP6, *The Cryosphere*, 13, 1441–1471,
773 <https://doi.org/10.5194/tc-13-1441-2019>, 2019.

774 Shackleton, C., Matsuoka, K., Moholdt, G., Van Liefferinge, B., and Paden, J.: Stochastic
775 Simulations of Bed Topography Constrain Geothermal Heat Flow and Subglacial Drainage
776 Near Dome Fuji, East Antarctica, *J. Geophys. Res. Earth Surf.*, 128, e2023JF007269,
777 <https://doi.org/10.1029/2023JF007269>, 2023.

778 Shapiro, N.: Inferring surface heat flux distributions guided by a global seismic model: particular
779 application to Antarctica, *Earth Planet. Sci. Lett.*, 223, 213–224,
780 <https://doi.org/10.1016/j.epsl.2004.04.011>, 2004.

781 Shen, W., Wiens, D. A., Lloyd, A. J., and Nyblade, A. A.: A Geothermal Heat Flux Map of Antarctica
782 Empirically Constrained by Seismic Structure, *Geophys. Res. Lett.*, 47, e2020GL086955,
783 <https://doi.org/10.1029/2020GL086955>, 2020.

784 Siahaan, A., Smith, R. S., Holland, P. R., Jenkins, A., Gregory, J. M., Lee, V., Mathiot, P., Payne, A.
785 J., Ridley, J. K., and Jones, C. G.: The Antarctic contribution to 21st-century sea-level rise
786 predicted by the UK Earth System Model with an interactive ice sheet, *The Cryosphere*, 16,
787 4053 – 4086, <https://doi.org/10.5194/tc-16-4053-2022>, 2022.

788 Smith-Johnsen, S., Schlegel, N. -J., De Fleurian, B., and Nisancioglu, K. H.: Sensitivity of the
789 Northeast Greenland Ice Stream to Geothermal Heat, *J. Geophys. Res. Earth Surf.*, 125,
790 e2019JF005252, <https://doi.org/10.1029/2019JF005252>, 2020.

791 Stål, T., Reading, A. M., Halpin, J. A., and Whittaker, J. M.: Antarctic Geothermal Heat Flow Model:
792 Aq1, *Geochem. Geophys. Geosystems*, 22, e2020GC009428,
793 <https://doi.org/10.1029/2020GC009428>, 2021.

794 Sun, S., Cornford, S. L., Moore, J. C., Gladstone, R., and Zhao, L.: Ice shelf fracture
795 parameterization in an ice sheet model, *The Cryosphere*, 11, 2543–2554,
796 <https://doi.org/10.5194/tc-11-2543-2017>, 2017.

797 Tsai, V. C., Stewart, A. L., and Thompson, A. F.: Marine ice-sheet profiles and stability under
798 Coulomb basal conditions, *J. Glaciol.*, 61, 205–215, <https://doi.org/10.3189/2015JoG14J221>,
799 2015.

800 Van Liefferinge, B., Pattyn, F., Cavitte, M. G. P., Karlsson, N. B., Young, D. A., Sutter, J., and Eisen,
801 O.: Promising Oldest Ice sites in East Antarctica based on thermodynamical modelling, *The*



802 Cryosphere, 12, 2773–2787, <https://doi.org/10.5194/tc-12-2773-2018>, 2018.

803 Weertman, J.: On the Sliding of Glaciers, J. Glaciol., 3, 33–38,
804 <https://doi.org/10.3189/S0022143000024709>, 1957.

805 Young, D. A., Schroeder, D. M., Blankenship, D. D., Kempf, S. D., and Quartini, E.: The distribution
806 of basal water between Antarctic subglacial lakes from radar sounding, Philos. Trans. R. Soc.
807 Math. Phys. Eng. Sci., 374, 20140297, <https://doi.org/10.1098/rsta.2014.0297>, 2016.

808 Zhao, C., Gladstone, R. M., Warner, R. C., King, M. A., Zwinger, T., and Morlighem, M.: Basal
809 friction of Fleming Glacier, Antarctica – Part 1: Sensitivity of inversion to temperature and
810 bedrock uncertainty, The Cryosphere, 12, 2637–2652, <https://doi.org/10.5194/tc-12-2637-2018a>, 2018a.

811 Zhao, L., Moore, J. C., Sun, B., Tang, X., and Guo, X.: Where is the 1-million-year-old ice at Dome
812 A?, The Cryosphere, 12, 1651–1663, <https://doi.org/10.5194/tc-12-1651-2018>, 2018b.

813 Zhang, X., Dong, X., Zeng, J., Hou, S., Smeets, P., Reijmer, C. H., and Wang, Y.: Spatiotemporal
814 Reconstruction of Antarctic Near-Surface Air Temperature from MODIS Observations, J.
815 Clim., 35, 5537–5553, 2022.

816 Zwinger, T., Schäfer, M., Martín, C., and Moore, J. C.: Influence of anisotropy on velocity and age
817 distribution at Scharffenbergbotnen blue ice area, The Cryosphere, 8, 607–621,
818 <https://doi.org/10.5194/tc-8-607-2014>, 2014.

819

820